Adsorption Behavior of a Ternary Covalent Organic Polymer Anchored with SO₃H for Ciprofloxacin

Zhuoran Wang [1,2,3,*], Chuanyu Qin [1,2,3], Dongyu Zhao [1,2,3], Ziheng Wang [1,2,3] and Dongpeng Mao [1,2,3]

[1] Key Laboratory of Groundwater Resources and Environment of Ministry of Education, College of New Energy and Environment, Jilin University, Changchun 130021, China; qincyu@jlu.edu.cn (C.Q.); zhaody20@mails.jlu.edu.cn (D.Z.); wzh20@mails.jlu.edu.cn (Z.W.); maodp20@mails.jlu.edu.cn (D.M.)

[2] Jilin Provincial Key Laboratory of Water Resources and Environment, College of New Energy and Environment, Jilin University, Changchun 130021, China

[3] National and Local Joint Engineering Laboratory for Petrochemical Contaminated Site Control and Remediation Technology, Jilin University, Changchun 130021, China

* Correspondence: zrwang20@mails.jlu.edu.cn

Abstract: Owing to the poor treatment efficiency of wastewater containing fluoroquinolones (FQs), effective removal of such pollutants has become a significant issue in waste management. In this study, a ternary covalent organic polymer anchored with SO₃H (COP-SO₃H) was designed using the Schiff reaction and a multicomponent solvent thermal method. The synthesized COP-SO₃H polymer possesses multiple functional binding sites, including amide groups, sulfonic groups, and aromatic frameworks, enabling it to effectively adsorb ciprofloxacin (which belongs to FQs) through mechanisms such as pore-filling effects, electrostatic interactions, hydrogen bonding, π-π electron donor–acceptor (EDA) interactions, and hydrophilic–lipophilic balance. COP-SO₃H demonstrated outstanding adsorption performance for ciprofloxacin, exhibiting a high adsorption capacity, broad pH stability, strong resistance to ionic interference, and good regenerability. Moreover, it displayed preferential selectivity toward fluoroquinolone antibiotics. The present study not only investigates the intricate structural and functional design of COP-SO₃H materials but also presents potential applications for the efficient adsorption of specific antibiotics.

Keywords: covalent organic polymers; ciprofloxacin; kinetic analysis; selective adsorption

1. Introduction

Fluoroquinolones (FQs) are a primary category of pharmaceutical compounds that exhibit high antibacterial efficacy and are widely used in disease treatment, infection prevention, and other areas [1,2]. Among these, ciprofloxacin (CIP), a third-generation FQ antibiotic and a prominent representative of the quinolone antibiotic class, is widely employed in livestock farming, healthcare, and aquaculture because of its cost-effectiveness, notable therapeutic benefits, and wide antibacterial coverage. Approximately 70% of these antibiotics are not metabolized and enter the environment through feces and urine [3]. CIP has been detected in diverse water bodies, including wastewater from hospitals, pharmaceutical manufacturers, residential areas, and rivers, with concentrations ranging from micrograms to milligrams per liter. Furthermore, research has indicated that the concentration of CIP in pharmaceutical factory effluents can exceed 31 mg·L^{-1}, posing a significant threat to human health [4,5]. In recent years, prolonged consumption of drinking water containing CIP has led to symptoms such as anxiety, nausea, vomiting, headaches, diarrhea, and tremors [6]. High concentrations of CIP can damage the human immune system, leading to conditions such as acute renal failure, elevated liver enzyme levels, and reduced white blood cell counts [7]. Additionally, CIP inhibits the growth of photoautotrophic aquatic organisms and exhibits high toxicity at certain concentrations [8]. When exposed to residual antibiotics and their metabolic degradation products, aquatic

bacteria in water environments develop resistance genes, which accelerate the development of bacterial resistance [9].

Given that CIP is continuously released into surface waters from wastewater treatment plants, agricultural runoff, aquaculture, and pharmaceutical manufacturing sites and subsequently enters the environment and threatens human health, it has become a popular research topic in the field of water environment remediation [10,11]. Various methods have been developed to remove CIP from water, including advanced oxidation processes [12], electrocoagulation [13], photodegradation [14], biodegradation [15], and adsorption [16]. Among these, the adsorption technique is distinguished by its cost-effectiveness, straightforward design, high efficiency, and compatibility with other water treatment systems. The choice of adsorbent material significantly affects the adsorption rate [17]. Thus far, inexpensive materials, such as silica dioxide, clay, zeolite, and bentonite, have been used to remove antibiotics from water. However, adsorbents commonly exhibit low porosity, small specific surface area, weak surface charge, low capacity, and poor selectivity, which ultimately diminish their removal efficiency of quinolone antibiotics [18,19]. Consequently, there has been widespread focus on designing adsorbents with exceptional extraction capabilities and significant selectivity based on the target molecular structure and physical characteristics to address these limitations [20,21].

Covalent organic polymers (COPs) are organic porous substances composed of light components, such as C, N, O, and H. The synthesis of various crystalline and amorphous COPs has been achieved, encompassing covalent organic frameworks (COFs) [22,23], covalent triazinyl frameworks (CTFs) [24], and microporous organic polymers (MOPs) [25]. Because of their strong chemical tunability, high crystallinity, adjustable pore structure, low density, and excellent stability, they are frequently employed in energy storage, gas adsorption and storage, and multiphase catalysis. Currently, sulfonated H-COF-SO_3H exhibits selective adsorption towards paraquat and dipyridine-containing polar cations through electrostatic interactions [26]. MOPs based on the Schiff base (SNW-1) can serve as enrichment coatings for the collection of volatile fatty acids in tea and tobacco powder samples [27]. Therefore, COPs demonstrate promising adsorption performance and application prospects. However, reports on the utilization of COPs as adsorbents in antibiotic wastewater treatment are limited, particularly regarding the selective adsorption of FQs. FQ antibiotics commonly possess a molecular structure featuring two ion-binding sites, a carboxyl group, and an amine group [1]. Based on this characteristic, an adsorbent with a specific affinity towards FQs was designed to achieve efficient and selective capture of FQ antibiotics while avoiding interference from other pollutants on its adsorption performance and enhancing its overall efficiency.

To accomplish our objective, a solvothermal method was employed to prepare a porous material (COP-SO_3H) featuring micropores and mesoporous pores. These pores serve as channels and pathways for diffusion within the adsorbent. Micropores and mesopores provide pathways for the diffusion of the adsorbate into the adsorbent material. The introduction of a sulfonic acid group and a -CO-NH- group to the adsorbent and electrostatic interactions between COP-SO_3H and FQs are expected to enhance the selectivity for FQs and effectively remove FQs present in water. The adsorption mechanism is mainly based on the pore-filling effect, electrostatic interactions, hydrogen bonding, π-π EDA interactions, and hydrophilic–lipophilic equilibrium. To verify the adsorption mechanism, the adsorption behavior of a new covalent organic polymer, COP-SO_3H, on FQs in water (taking CIP as an example) was examined in this study, and detailed information on the adsorption capacity, adsorption kinetics, adsorption thermodynamics, and adsorption mechanism was obtained. The present study not only investigated the selective adsorption of sulfonic acid groups and amide bonds on FQs in covalent organic polymers, but also proposed a novel approach for designing the removal of organic pollutants from water.

2. Results and Discussion

2.1. Synthesis and Characterization of COP-SO3H

As shown in Figure 1, COP-SO$_3$H was prepared by connecting BTCH, TPDA, and DABA via imine bonds, using a solvothermal method. Figure 2B shows the physical appearance of COP-SO$_3$H. Figure 2A,H shows the scanning electron microscopy (SEM) and transmission electron microscopy (TEM) analyses revealing the amorphous nature of COP-SO$_3$H, characterized by an internal honeycomb structure. Furthermore, elemental mapping based on energy-dispersive X-ray spectroscopy (EDX) confirmed the uniform distribution of C, N, O, and S on the surface of COP-SO$_3$H, as shown in Figure 2C–F,I–L. The elemental analysis, as illustrated in Table 1, demonstrates congruence between the measured and theoretical values. Notably, the presence of S confirmed the successful anchoring of sulfonic acid groups onto COP-SO$_3$H.
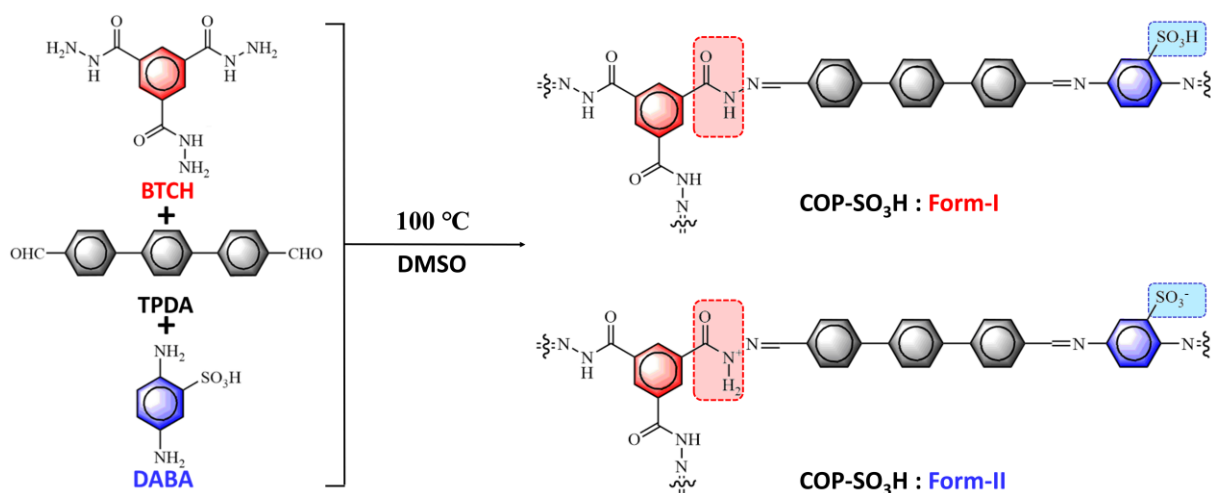

Figure 1. Schematic diagram of COP-SO$_3$H synthesis.

Table 1. Elemental analysis of COP-SO$_3$H.

Materials	C (wt %)		H (wt %)		N (wt %)		S * (wt %)	
	Calc.	Exp.	Calc.	Exp.	Calc.	Exp.	Calc.	Exp.
COP-SO$_3$H	66.92	74.17	3.85	4.91	10.76	6.58	6.15	0.62

* Instrument error results in discrepancy in the measurement of S content.

The structure of COP-SO$_3$H was further investigated using 13C CP/MAS NMR (Figure 3) and FTIR (Figure 4A) characterization techniques. The FT-IR spectra exhibited characteristic peaks at 3290 and 3338 cm^{-1} for BTCH and DABA, respectively. Notably, the N–H stretching band (3290–3338 cm^{-1}) was absent in COP-SO$_3$H [28]. A new characteristic peak emerged at 1545 cm^{-1}, attributed to imine bond formation [29], coinciding with the disappearance of the BTCH and DABA peaks, thus confirming the successful synthesis of COP-SO$_3$H. Furthermore, the new peak at 1003 cm^{-1} in COP-SO$_3$H indicates the stretching band of the sulfonic acid groups [28]. The solid-state ^{13}C NMR spectrum of COP shows peaks at 163 ppm, which can be assigned to imine carbon and amide carbon, indicating the successful synthesis of COP [30].
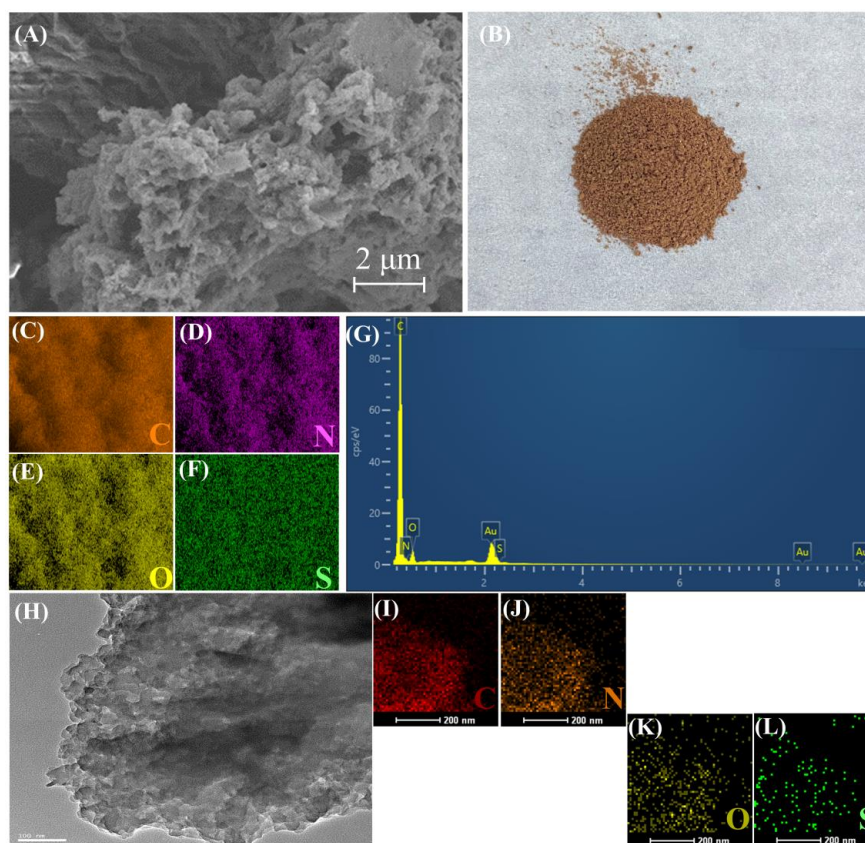
Figure 2. (**A**) SEM image of COP-SO$_3$H. (**B**) Photograph of COP-SO$_3$H. (**C–F**) EDX elemental mapping of C, N, O, and S. (**G**) EDS spectrum of COP-SO$_3$H. (**H**) TEM image of COP-SO$_3$H. (**I–L**) TEM elemental mapping of C, N, O, and S.
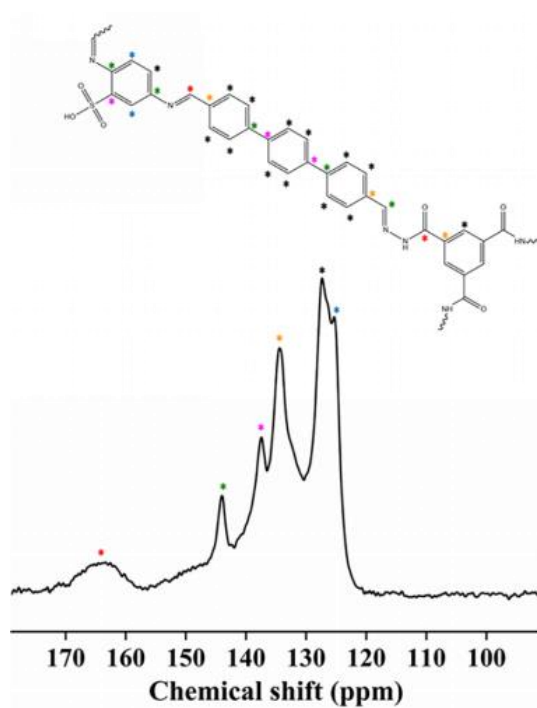
Figure 3. Solid-state ^{13}C CP/MAS NMR spectra of COP-SO$_3$H. The red stars represent carbons of imine bonds, the green stars represent carbons linked to N and benzene rings, and the others are attributed to other aromatic carbons.

Figure 4. (**A**) BTCH, DABA, and COP-SO$_3$H FT-IR spectra. (**B–E**) XPS spectra of O 1s, C 1s, N 1s, and S 2p in COP-SO$_3$H. (**F**) Adsorption–desorption curves and pore size distribution of COP-SO$_3$H. (**G**) TGA curve of COP-SO$_3$H. (**H**) XRD spectra of COP-SO$_3$H, HCl@COP-SO$_3$H, and NaOH@COP-SO$_3$H.

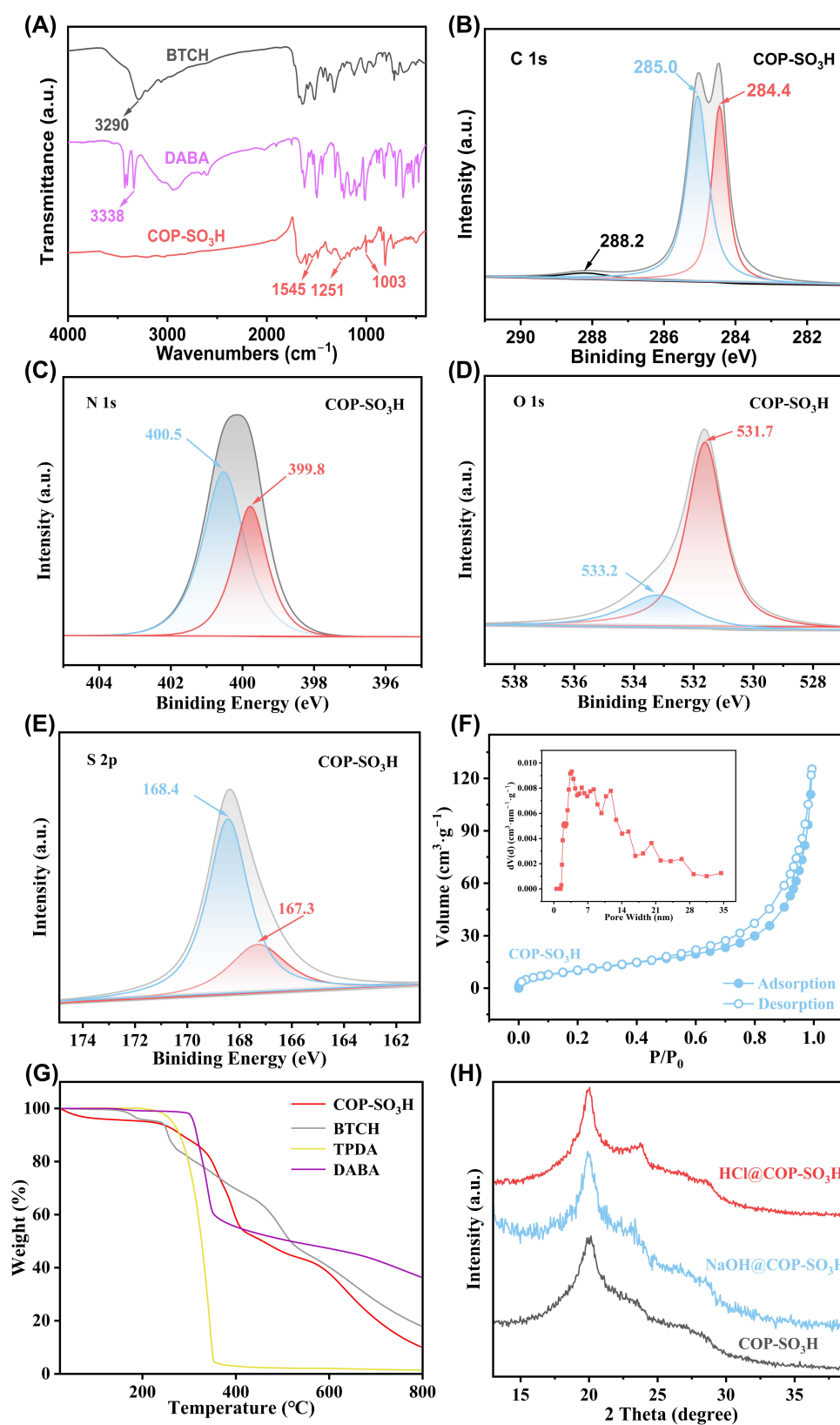The chemical elements and their states in the adsorbents were investigated via XPS analysis, which confirmed the successful synthesis of COP-SO$_3$H. The XPS spectra of C, N, O, and S in COP-SO$_3$H (Figure 4B–E) corresponded to the expected components. For C, the 1s peaks at 288.2, 258.0, and 284.4 represent C=O, C-S/C=N, and C-C/C=C, respectively [31]. The N elements exhibit 1s peaks at 400.5 and 399.8 eV, attributed to the formation of amine bonds in COP-SO$_3$H [32]. For O elements, the 1s binding energy peaks at 533.2 and 531.7 eV indicate the presence of C=O and S=O groups in COP-SO$_3$H [33]. Notably, COP-SO$_3$H exhibited two distinct configurations. For S, the 1s binding energy spectrum of COP-SO$_3$H reveals two peaks (168.4 and 167.3 eV), corresponding to sulfonic acid groups (SO$_3$H) and sulfonate ions (SO$_3^-$). The 1s peak at 400.5 eV for N originates from the protonated secondary amine (-NH^{2+}) within the Form-II structure [28].

Nitrogen adsorption–desorption tests (Figure 4F) were conducted at 77 K to determine the specific surface area of COP-SO$_3$H. The BET isotherm exhibits a typical type-IV shape [34]. The BET surface area of COP-SO$_3$H was calculated as 44.77 m$^2 \cdot$g^{-1}, and the pore size distribution was primarily concentrated at approximately 1.25 nm and 3.5–7 nm, indicating that COP-SO$_3$H is a porous material containing both micro- and meso-pores. Furthermore, the thermal and chemical stabilities of COP-SO$_3$H were examined via thermogravimetric analysis (TGA) under a nitrogen atmosphere. The TGA results (Figure 4G) indicate that COP-SO$_3$H maintained stability up to 336.1 °C. Moreover, immersing COP-SO$_3$H in HCl (3 M) and NaOH (3 M) solutions revealed that HCl@COP-SO$_3$H and NaOH@COP-SO$_3$H exhibited XRD patterns (Figure 4H) consistent with those of pristine COP-SO$_3$H, revealing no new diffraction peaks. This result aligns with the amorphous nature of COP-SO$_3$H and confirms its high stability under extreme conditions.

2.2. Batch-Wise Adsorption Experiments

2.2.1. Effect of Adsorbent Dosage on Adsorption Performance

The influence of adsorbent dosage on the removal efficiency of CIP was further assessed to optimize the COP-SO$_3$H dosage for the experiments, aiming to maintain cost-effectiveness and pollutant removal efficacy. The COP-SO$_3$H loading ratio (ratio of material mass to CIP solution volume) was varied across five gradients, ranging from 0.25 g$\cdot$L^{-1} to 2 g$\cdot$L^{-1}, for the adsorption experiments. The aforementioned material was added to a 50 mL centrifuge tube, followed by 20 mL of pollutant solution at a concentration of 10 mg$\cdot$L^{-1}. Subsequently, the mixture was placed on an open-air orbital shaker and agitated for 24 h. Subsequently, the concentration of FQ was determined. The results shown in Figure 5A indicate that, as the adsorbent dosage increased, the removal efficiency gradually increased from 67.92% to 95.97%. This trend can be attributed to the increase in the effective surface area and adsorption sites of the material for pollutants [35]. However, because the amount of pollutants in the system remains fixed, excessive addition of adsorbent material results in the aggregation of adsorbent particles [36]. This leads to unoccupied adsorption sites, where pollutants remain uncaptured, rendering an increased dosage of adsorbent material only marginally effective in enhancing the removal efficiency of CIP [37]. Consequently, the CIP removal efficiency slowly increased when the dosage was between 1 and 2 g$\cdot$L^{-1}. Considering the removal efficiency and experimental cost, the optimal COP-SO$_3$H dosage was 1.0 g$\cdot$L^{-1}.
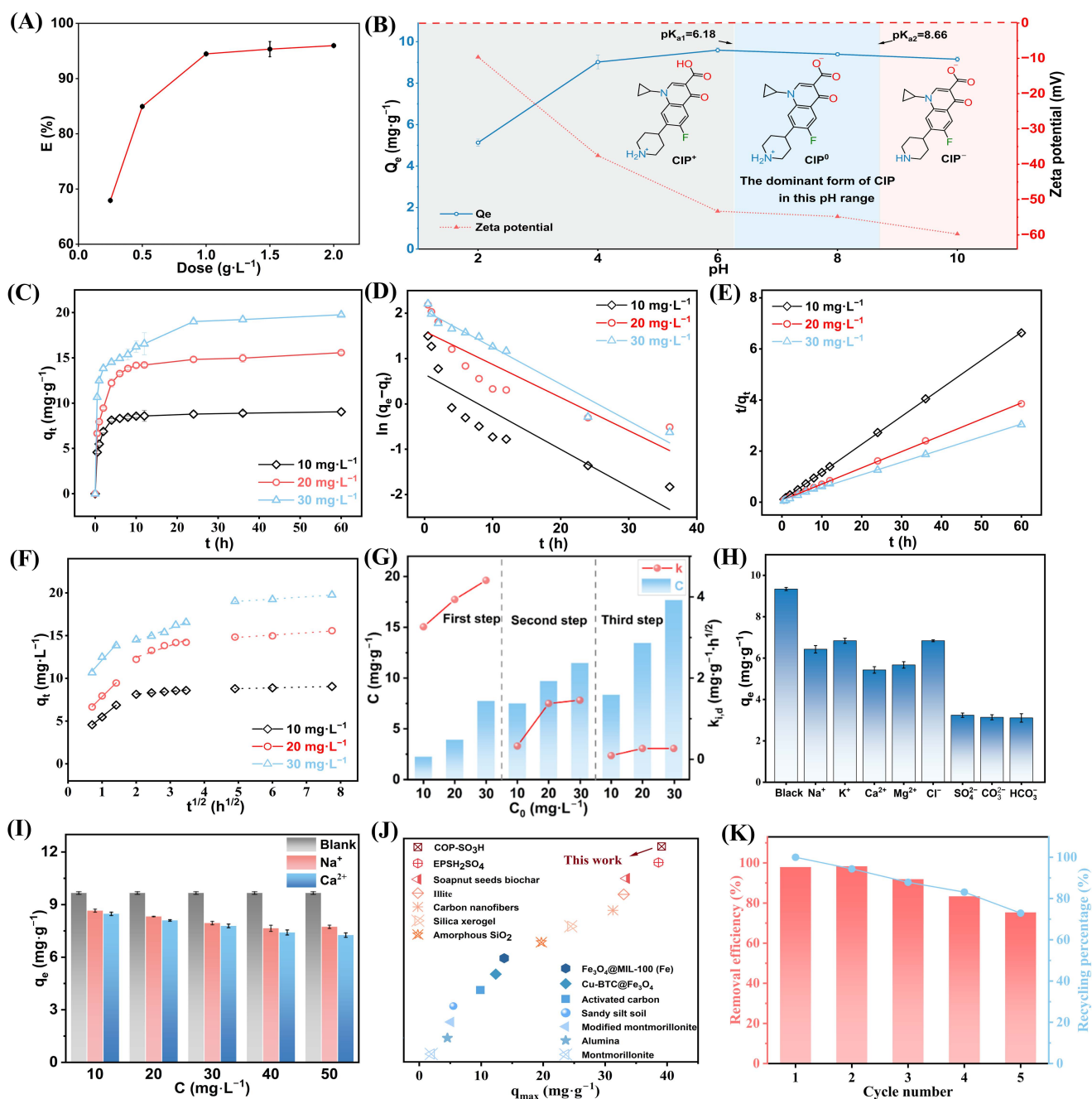
Figure 5. (**A**) Impact of dosage on CIP adsorption onto COP-SO$_3$H. (**B**) Influence of pH on CIP adsorption and zeta potential of COP-SO$_3$H. (**C**) Kinetic study of CIP adsorption onto COP-SO$_3$H at 10, 20, and 30 mg·L^{-1} initial concentrations. (**D**) Pseudo-first-order kinetics of COP-SO$_3$H for CIP adsorption at different concentrations. (**E**) Pseudo-second-order kinetics of COP-SO$_3$H for CIP adsorption at different concentrations. (**F**) Intra-particle diffusion model for CIP adsorption onto COP-SO$_3$H. (**G**) Different intra-particle diffusion model parameters (C and K$_{i,d}$) with concentration. (**H**) Effect of various inorganic ions on CIP adsorption onto COP-SO$_3$H. (**I**) Influence of ionic strength on CIP adsorption onto COP-SO$_3$H. (**J**) Comparison of the maximum adsorption capacities for CIP. (**K**) Results of five continuous cycles of reusing COP-SO$_3$H for CIP adsorption.

2.2.2. Effect of pH on Adsorption Performance

During operation, wastewater treatment plants must treat sewage at various pH levels. Therefore, the adsorbent must efficiently capture antibiotics over a wide pH range, making the pH value of wastewater a significant reference factor influencing the adsorption process.

Figure 5B shows the impact of pH (ranging from 2.0 to 10.0) on the adsorption capacity of COP-SO$_3$H for CIP. At an initial CIP concentration of 10 mg·L^{-1} and a temperature of 293 K, the equilibrium adsorption capacity (q$_e$) of CIP on COP-SO$_3$H increased from 5.1 mg·L^{-1} to 9.6 mg·L^{-1} as the pH increased, and then slightly decreased to 9.15 mg·L^{-1}. Notably, CIP exists in three forms, depending on the pH: cationic (CIP$^+$) at pH < 6.18, anionic (CIP$^-$) at pH > 8.15, and zwitterionic (CIP^0) at 6.18 < pH < 8.15. The zeta potential of COP-SO$_3$H was negatively charged and increased with increasing pH. Based on the experimental results, as the pH increased from 4 to 6, the negative charge of COP-SO$_3$H significantly strengthened, increasing the adsorption capacity. As the pH approached neutrality, the strong hydrophobic interaction between CIP^0, CIP$^\pm$, and COP-SO$_3$H, coupled with enhanced π–π electron donor–acceptor (EDA) interactions due to electrostatic attraction, significantly increased the adsorption affinity between them. Conversely, strong electrostatic repulsion weakened the π–π EDA interaction, thereby inhibiting the adsorption effectiveness of COP-SO$_3$H for CIP. Therefore, the influence of pH on the CIP adsorption capacity of COP-SO$_3$H depends on the balance between the electrostatic, hydrophobic, and π-π EDA interactions. Because q$_e$ peaked at pH 6, this pH level was selected as the most suitable for our experiments.

2.2.3. Influence of Contact Time on Adsorption/Adsorption Kinetics

To evaluate the impact of contact time on adsorption, 1 g·L^{-1} CIP solutions with initial concentrations of 10, 20, and 30 mg·L^{-1} were exposed to COP-SO$_3$H for varying durations. The temperature was maintained at 20 °C. Figure 5C shows that the equilibrium time for CIP adsorption onto COP-SO$_3$H is within 24 h for all three initial concentrations. The adsorption capacities of COP-SO$_3$H for CIP with initial concentrations of 10, 20, and 30 mg·L^{-1} were 9.05, 15.57, and 19.76 mg·L^{-1}, respectively. These results indicated that increasing the initial CIP concentration enhanced the adsorption capacity.

Three kinetic models were fitted to the data to understand the adsorption process and mechanism: pseudo-first-order, pseudo-second-order, and intra-particle diffusion models. The equations used are as follows [38–40]:

$$\frac{dq_t}{dt} = k_1(q_e - q_t) \tag{1}$$

$$n(q_e - q_t) = \ln q_e - k_1 t \tag{2}$$

$$\frac{dq_t}{dt} = k_2(q_e - q_t)^2 \tag{3}$$

$$\frac{t}{q_t} = \frac{1}{q_e}t + \frac{1}{k_2 q_e^2} \tag{4}$$

$$q_t = k_{i,d} t^{1/2} + C_i \tag{5}$$

where q$_e$ (mg) and q$_t$ (mg) represent the adsorption amounts of CIP on COP-SO$_3$H at equilibrium and time t, respectively, k$_1$ (h^{-1}) is the first-order adsorption rate constant, k$_2$ (g·mg^{-1}·h^{-1}) is the second-order adsorption rate constant, and C$_i$ (mg·g^{-1}) is the parameter representing the thickness of the adsorbed CIP layer.

Based on the fitting results (Figure 5D,E and Table 2), the pseudo-second-order model demonstrated a stronger fit (R^2 > 0.99) than the pseudo-first-order model. Additionally, the experimentally determined adsorption capacities (q$_{e,exp}$) closely aligned with the calculated values (q$_{e,cal}$) from the pseudo-second-order model, indicating that it describes the adsorption process of CIP onto COP-SO$_3$H more accurately than the pseudo-first-order kinetic model. These results underscore that chemical adsorption is the primary mechanism governing CIP adsorption onto COP-SO$_3$H.

Table 2. Kinetic parameters for CIP adsorption by COP-SO$_3$H.

C_0	$q_{e,exp}$	Removal Efficiency	Pseudo-First-Order Dynamics Model				Pseudo-Second-Order Dynamics Model			
(mg·L^{-1})	(mg·g^{-1})		$q_{e,cal}$	k_1	Δq_1	R^2	$q_{e,cal}$	k_1	Δq_1	R^2
		(%)	(mg·g^{-1})	(h^{-1})	(%)		(mg·g^{-1})	(h^{-1})	(%)	
10	9.05	90.50	1.92	0.082	370.3	0.71	9.11	0.170	0.65	0.99
20	15.57	77.85	4.96	0.073	214.0	0.74	15.73	0.057	1.01	0.99
30	19.76	65.87	7.83	0.081	152.3	0.96	20.12	0.033	1.79	0.99

Intra-particle diffusion analysis (Figure 5F and Table 3) revealed a three-stage diffusion process of CIP within COP-SO$_3$H. The initial stage is the external diffusion phase, where the adsorption rate $k_{i,1}$ reached its maximum at the same concentration, indicating rapid adsorption. This suggests that CIP molecules migrated from the solution to the external surface of COP-SO$_3$H during initial adsorption. The second stage is the internal diffusion phase, with the adsorption rate $k_{i,1} > k_{i,2}$, indicating gradual adsorption. This suggests that the CIP molecules saturated the external surface of COP-SO$_3$H and diffused from the outer surface to the inner surface of the material. The third stage is the desorption–adsorption equilibrium phase, where the adsorption rate $k_{i,2} > k_{i,3} \approx 0$. This indicated that the CIP molecules reached saturation on both the external and internal surfaces of COP-SO$_3$H, and the desorption and adsorption of CIP molecules reached equilibrium. However, none of the diffusion curves passed through the origin, suggesting that the entire adsorption process was influenced by multiple steps [41].

Table 3. Intra-particle diffusion model parameters for CIP adsorption by COP-SO$_3$H.

C_0	Intraparticle Diffusion Model								
(mg·L^{-1})	$k_{i,1}$	C_1	R^2	$k_{i,2}$	C_2	R^2	$k_{i,3}$	C_3	R^2
	(mg·g^{-1}·h$^{-1/2}$)	(mg·g^{-1})		(mg g^{-1} h$^{-1/2}$)	(mg·g^{-1})		(mg·g^{-1}·h$^{-1/2}$)	(mg·g^{-1})	
10	3.26	2.25	0.99	0.33	7.50	0.96	0.09	8.35	0.99
20	3.94	3.92	0.99	1.37	9.72	0.89	0.27	13.47	0.91
30	4.41	7.74	0.99	1.46	11.48	0.96	0.27	17.68	0.97

2.2.4. Adsorption Isotherms and Thermodynamics

This section explores the maximum CIP adsorption capacity of COP-SO$_3$H and its interactions. The adsorption results at CIP concentrations ranging from 10 to 170 mg·L^{-1} under three different temperature conditions (10, 20, and 30 °C) were investigated. The experimental data were fitted using single-layer Langmuir and multi-layer Freundlich adsorption isotherm models (Figure 6A,B), as represented by Equations (6) to (8) [42,43]:

$$\frac{C_e}{q_e} = \frac{1}{K_L q_m} + \frac{C_e}{q_m} \tag{6}$$

$$R_L = \frac{1}{1 + K_L C_0} \tag{7}$$

$$q_e = K_F C_e^{1/n} \tag{8}$$

where q_e (mg·g^{-1}) represents the adsorption capacity of the adsorbent for the adsorbate CIP at adsorption equilibrium, C_e (mg·g^{-1}) is the residual concentration of CIP in the solution at adsorption equilibrium, q_m (mg·g^{-1}) denotes the theoretical maximum adsorption capacity per unit mass of adsorbent COP-SO$_3$H, K_L (L·mg^{-1}) is the Langmuir equilibrium constant, $1/n$ represents the adsorption intensity, and R_L indicates the difficulty level of the adsorption process.
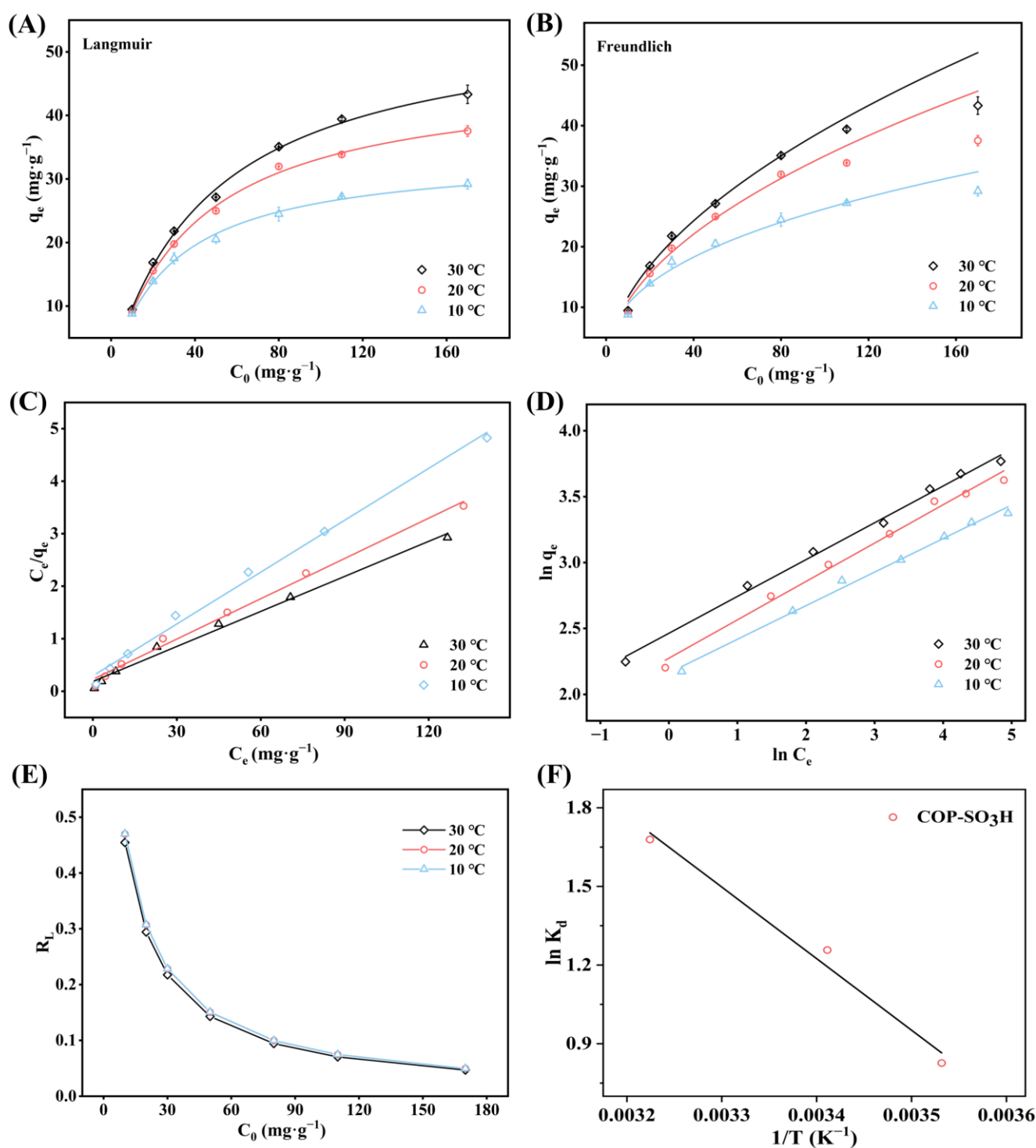
Figure 6. (**A**,**B**) Adsorption isotherms of COP-SO$_3$H for CIP at 10, 20, and 30 °C. (**C**) Langmuir linear adsorption fit of COP-SO$_3$H for CIP at 10, 20, and 30 °C. (**D**) Freundlich linear adsorption fit of COP-SO$_3$H at 10, 20, and 30 °C. (**E**) Relationship between R$_L$ and initial concentration. (**F**) Thermodynamic fit of CIP adsorption onto COP-SO$_3$H.

The results indicated a significant increase in the adsorption capacity of COP-SO$_3$H for CIP with higher initial concentrations under the same temperature conditions. This trend suggests that elevated initial concentrations promote CIP adsorption onto COP-SO$_3$H by creating a larger concentration difference, thereby acting as a pivotal driving force for adsorption [44,45]. This reduction in the mass transfer resistance between CIP

in the solution and COP-SO$_3$H enhanced the overall efficiency. As shown in Table 4, the Langmuir model exhibited a better fit ($R^2 > 0.99$) than the Freundlich model, indicating that the single-layer adsorption mechanism better described the CIP adsorption process of COP-SO$_3$H. According to the Langmuir model, the theoretical maximum adsorption capacities of COP-SO$_3$H for CIP at 10, 20, and 30 °C were 30.37, 39.11, and 44.96 mg·g^{-1}, respectively. Importantly, COP-SO$_3$H exhibited superior adsorption performance compared to other adsorbents, such as modified montmorillonite, sandy silt soil, and carbon nanofibers (Figure 5J and Table 5), highlighting its value as a practical adsorbent. Furthermore, the calculated R$_L$ values for CIP adsorption onto COP-SO$_3$H at 10, 20, and 30 °C ranged from 0.047 to 0.470, falling between 0 and 1. This suggests that the adsorption equilibrium between COP-SO$_3$H and CIP promotes the adsorption process effectively.

Table 4. Adsorption parameters of isotherm models for the CIP adsorption by COP-SO$_3$H.

T	Langmuir Isotherm			Freundlich Isotherm		
(°C)	q$_m$	K$_L$	R^2	K$_F$	n	R^2
	(mg·g^{-1})	(L·mg^{-1})		(mg·g^{-1}) (L·mg^{-1})$^{1/n}$		
10	30.37	0.11	0.99	8.70	3.93	0.99
20	39.11	0.11	0.99	9.73	3.44	0.98
30	44.96	0.11	0.99	11.75	3.58	0.98

Table 5. Comparison of the maximum adsorption capacity of CIP by different adsorbents.

S.N.	Adsorbents	Adsorption Capacity (mg·g^{-1})	Conditions	Reference
1	Montmorillonite	1.94	298 K	[46]
2	Alumina	4.55	298 K	[46]
3	Modified montmorillonite	5.10	298 K	[46]
4	Sandy silt soil	5.50	298 K	[47]
5	Activated carbon	9.87	298 K	[46]
6	Cu-BTC@Fe$_3$O$_4$	12.35	298 K	[48]
7	Fe$_3$O$_4$@MIL-100 (Fe)	13.65	298 K	[49]
8	Amorphous SiO$_2$	19.71	298 K	[38]
9	Silica xerogel	24.45	298 K	[50]
10	Carbon nanofibers	31.26	298 K	[51]
11	Illite	33	/	[52]
12	Soapnut seeds biochar	33.44	303 K	[53]
13	EPS$_{H2SO4}$	38.61	/	[54]
14	COP-SO$_3$H	39.11	293 K	This work

Adsorption thermodynamics helps to understand the effect of temperature on the adsorption process and can further elucidate the adsorption mechanism of CIP onto COP-SO$_3$H. At different temperatures, the values of Gibbs' free energy change (ΔG^0, kJ·mol^{-1}), entropy change (ΔH^0, kJ·mol^{-1}), and enthalpy change (ΔS^0, kJ·mol^{-1}·K^{-1}) were calculated using Equations (9)–(11) as follows [55]:

$$\Delta G^0 = -RT \ln K_a \tag{9}$$

$$K_a = 10^6 K_L \tag{10}$$

$$\ln K_a = \frac{\Delta S^\circ}{R} - \frac{\Delta H^\circ}{RT} \qquad (11)$$

where R is the universal gas constant (8.3145 J·mol^{-1}·K^{-1}), and T is the solution temperature (K). K_a is the thermodynamic equilibrium constant without units, which can be obtained by multiplying Langmuir equilibrium constant K_L (L·mg^{-1}) by 10^6. As shown in Table 6, the values of ΔG^0 were negative at 10, 20, and 30 °C, indicating that the adsorption of CIP onto COP-SO$_3$H was spontaneous. With increasing temperature, the values of ΔG^0 decreased from -1.95 to -4.23 kJ·mol^{-1}, indicating that higher temperatures enhanced the adsorption performance of COP-SO$_3$H. This observation was consistent with the Langmuir model fitting results. Moreover, the obtained value of ΔH^0 suggested that the adsorption of CIP onto SO$_3$H was an endothermic process.

Table 6. Thermodynamic parameters for the CIP adsorption by COP-SO$_3$H.

Temperature (K)	ΔG^0 (kJ·mol^{-1})	ΔH^0 (kJ·mol^{-1})	ΔS^0 (kJ·mol^{-1}·K^{-1})
283	-1.95		
293	-3.06	22.69	0.08734
303	-4.23		

2.2.5. Influence of Inorganic Ion Type and Ionic Strength on Adsorption

To assess the impact of inorganic ions in the wastewater on the adsorption of CIP onto COP-SO$_3$H, eight ions were selected for experimentation: Na$^+$, K$^+$, Ca^{2+}, and Mg^{2+} (as cations) and Cl$^-$, SO$_4^{2-}$, CO$_3^{2-}$, and HCO$_3^-$ (as anions). The effects of different ion concentrations (10 mM) on CIP adsorption onto COP-SO$_3$H were also investigated. Notably, the hydrogen bonds between the oxygen acid ions and COP-SO$_3$H enhanced the affinity between these ions and CIP. Consequently, oxygen-containing acid ions suppressed the adsorption of CIP onto COP-SO$_3$H. Furthermore, the effects of the Na$^+$ and Ca^{2+} concentrations on adsorption were examined (Figure 5I). As the Na$^+$ and Ca^{2+} concentrations increased, the hydrophobic interactions between COP-SO$_3$H and CIP intensified. Simultaneously, the competition between CIP and Na$^+$ or Ca^{2+} resulted in a substantial initial decrease, followed by a plateau in the adsorption amount of COP-SO$_3$H for CIP.

2.2.6. Recyclability

The recyclability of adsorbents has economic value for wastewater treatment. Highly recyclable adsorbents contribute to both stability and cost reduction during practical use. Methanol was employed as a desorption agent for five consecutive adsorption–desorption cycles of CIP onto COP-SO$_3$H. Based on the results, the CIP removal efficiency of COP-SO$_3$H and its recovery efficiency in each cycle were investigated. The results indicated that the removal efficiency could reach 92% by the third cycle, and with an increase in the number of cycles to five, the removal efficiency of COP-SO$_3$H for CIP still remained at 75% (Figure 5K). SEM, FT-IR, and XRD analyses (Figure 7A–C) revealed no significant structural changes in COP-SO$_3$H after five cycles. This finding demonstrates that COP-SO$_3$H is a reusable adsorbent.
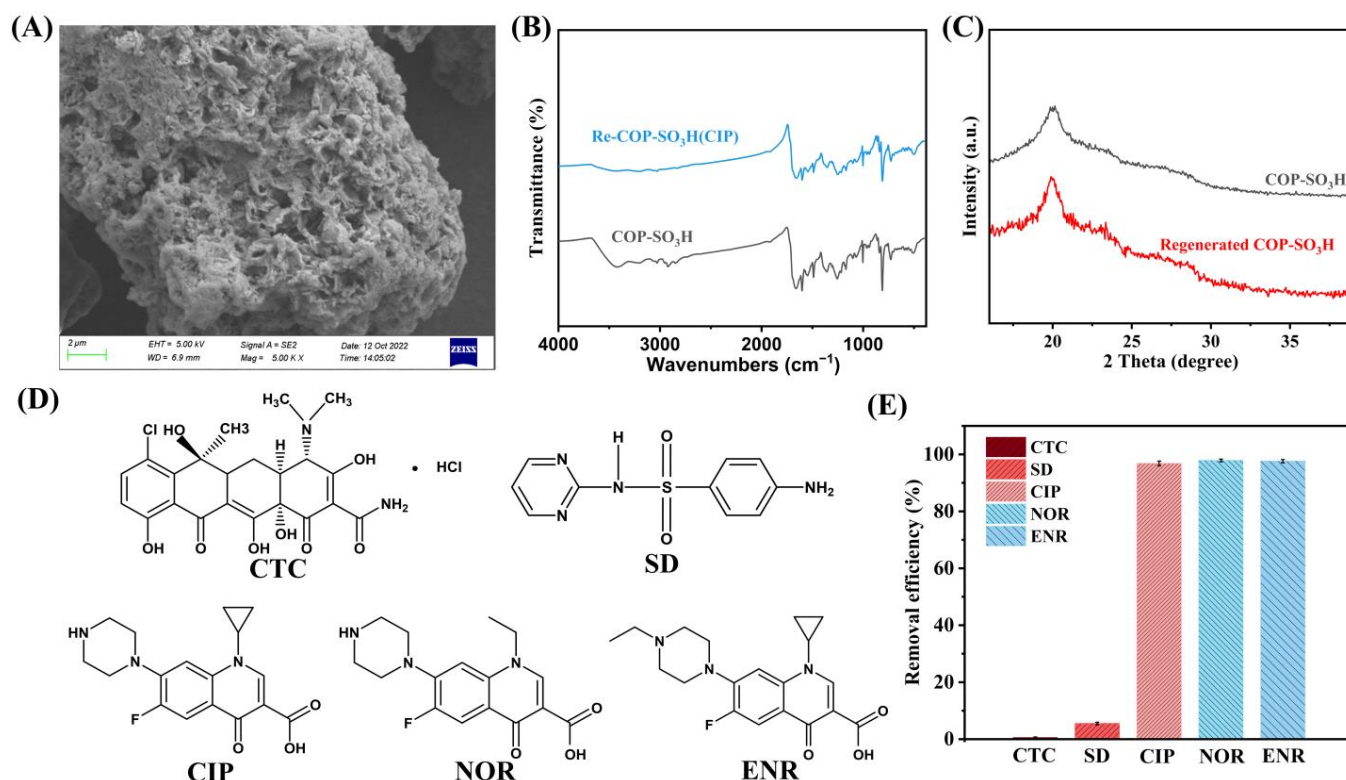
Figure 7. Regeneration of COP-SO$_3$H after five cycles of reuse: (**A**) SEM, (**B**) FT-IR spectra, and (**C**) XRD. (**D**) Structures of CTC, SD, CIP, NOR, and ENR. (**E**) Removal efficiency of COP-SO$_3$H for CTC, SD, CIP, NOR, and ENR.

2.2.7. Adsorption Selectivity

The applicability of a material to water treatment depends on its adsorption selectivity. To investigate the adsorption selectivity of COP-SO$_3$H, its efficiency in removing sulfonamide, tetracycline, and quinolone antibiotics was assessed at a pH of 6. Five antibiotics were selected, i.e., tetracycline (chlorotetracycline, CTC), sulfonamide (sulfadiazine, SD), and quinolones (ciprofloxacin, CIP; norfloxacin, NOR; and enrofloxacin, ENR). The structural formulae are shown in Figure 7D. When COP-SO$_3$H was used to adsorb each antibiotic, the removal efficiencies were 0.52%, 5.50%, 96.83%, 97.87%, and 97.61%, respectively (Figure 7E). COP-SO$_3$H exhibited a favorable adsorption performance for CIP, NOR, and ENR because of their similar chemical structures. The electrostatic interactions between Form-II of COP-SO$_3$H and quinolone antibiotics (FQs) resulted in a stronger affinity of COP-SO$_3$H for FQs than for other antibiotics. Consequently, the adsorption sites on the COP-SO$_3$H adsorbent exhibited selective binding capability for FQs.

3. Synthesis of COP-SO$_3$H

The porous structures are crucial for adsorption. The existence of pores serves as a precondition for various interactions and is a significant factor influencing the performance of porous adsorbents [56]. COP-SO$_3$H, with its microporous and mesoporous channel structures, can capture CIP. To explore the possibility of CIP entering the pores during adsorption, the adsorbed material (CIP@COP-SO$_3$H) underwent N$_2$ adsorption–desorption tests at 160 °C for 12 h. After adsorption, the BET surface area was reduced to 26.73 m^2·g^{-1}, indicating a 40% decrease, confirming CIP adsorption within the pores, which is known as the pore-filling effect.

According to the effects of the pH and various ions on the adsorption capacity of COP-SO$_3$H for CIP, as well as the zeta potential analysis, at a pH of 6, the zeta potential of CIP@COP-SO$_3$H (9.3 mV) was significantly higher than that of CIP@COP-SO$_3$H (9.3 mV), indicating that electrostatic interactions occurred during adsorption. Furthermore, analyz-

ing the XPS profiles before and after COP-SO₃H adsorbed CIP revealed that the peaks in the N 1s spectrum after adsorption shifted from binding energies of 400.5 and 399.8 eV to 400.6 and 399.6 eV, respectively. This suggests that electrostatic interactions occur between COP-SO₃H and CIP.

Even when subjected to weak electrostatic interactions between COP-SO₃H and CIP or strong electrostatic repulsions, the adsorption performance remained adequate. We speculate that other factors also affect the adsorption process. Notably, in the C 1s spectrum of COP-SO₃H, the peaks corresponding to the C=O bond (288.2 eV), C–S/C=N bond (258.0 eV), and C–C/C=C bond (284.4 eV) shifted to 287.7, 284.9, and 284.5 eV, respectively (Figure 8B). This can be attributed to the π-π EDA interactions between the electron-rich framework of COP-SO₃H and CIP molecules, which led to the capture of CIP. Additionally, a new peak at 687.9 eV in the CIP@COP-SO₃H spectrum indicates that COP-SO₃H may have captured the F element present in the CIP molecule.
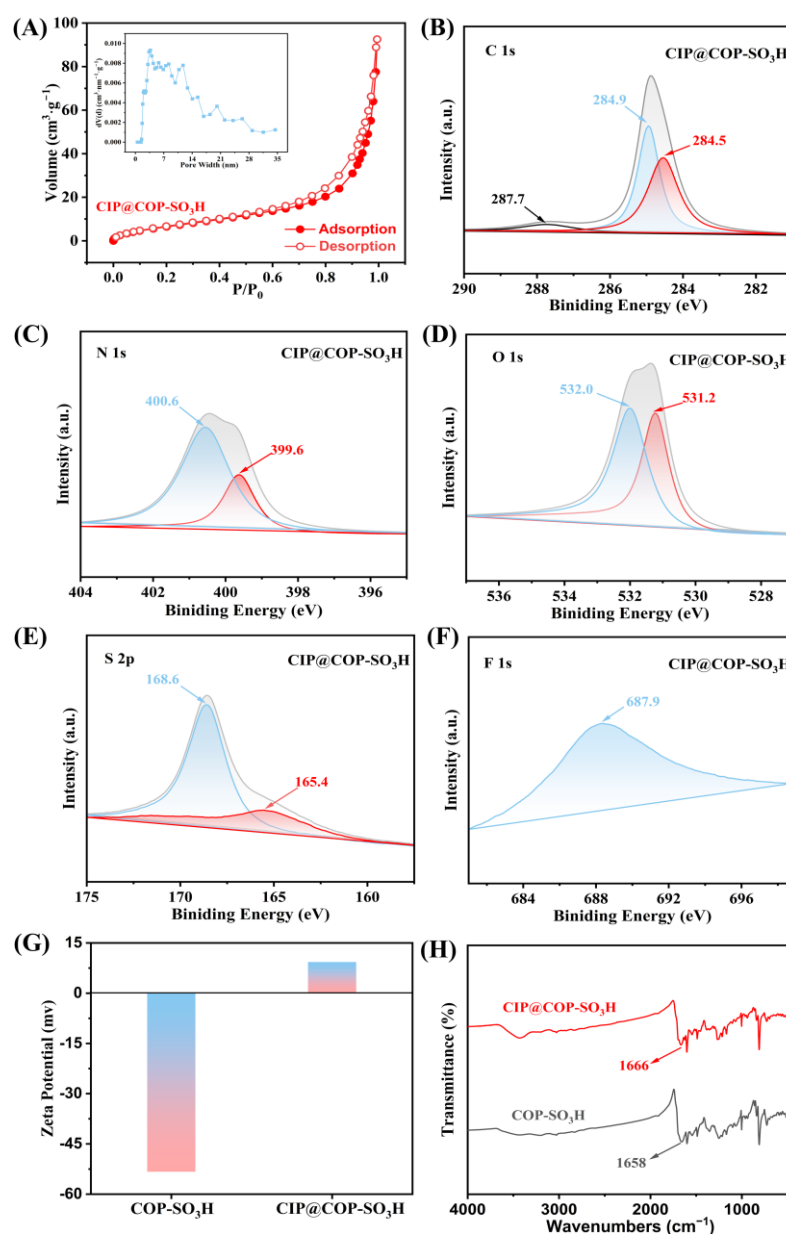

Figure 8. (**A**) Adsorption–desorption curves and pore size distribution of CIP@COP-SO₃H. (**B**–**F**) XPS spectra of C 1s, N1s, O1s, S2p, and F1s of CIP@COP-SO₃H. (**G**) Zeta potential values for COP-SO₃H and CIP@COP-SO₃H. (**H**) Infrared spectra of COP-SO₃H and CIP@COP-SO₃H.

Further analysis of the infrared spectra before and after the adsorption by COP-SO$_3$H (Figure 8H) revealed that the adsorption peak at 1658 cm^{-1}, associated with the C=O bond, shifted to 1666 cm^{-1}. This indicated hydrogen bonding interactions between the COP-SO$_3$H material and CIP. Specifically, the -SO$_3$H and -CO-NH- functional groups anchored onto the surface of the material demonstrated the capability to form hydrogen bonds with the -NH$_2$, -COOH, and -F functional groups present within the CIP structure.

Apart from the four interactions mentioned above, the hydrophilic–lipophilic balance in the adsorption process cannot be overlooked. Both the COP-SO$_3$H and CIP molecules contained several hydrophilic and hydrophobic groups. For instance, the carboxyl and hydroxyl groups in COP-SO$_3$H play a hydrophilic role when binding to CIP molecules, increasing the speed at which CIP enters the pores. Additionally, both the COP-SO$_3$H material and CIP molecules contained aromatic rings, which promoted hydrophobic interactions between the two. These two effects form a hydrophilic–lipophilic balance during adsorption [57].

In summary, a plausible mechanism for CIP adsorption on COP-SO$_3$H was inferred. This mechanism involves a combination of the pore-filling effect, electrostatic interactions, hydrogen bonding, π-π EDA interactions, and hydrophilic–lipophilic balance, all of which collectively determine the adsorption efficiency of the material (as illustrated in Figure 9).
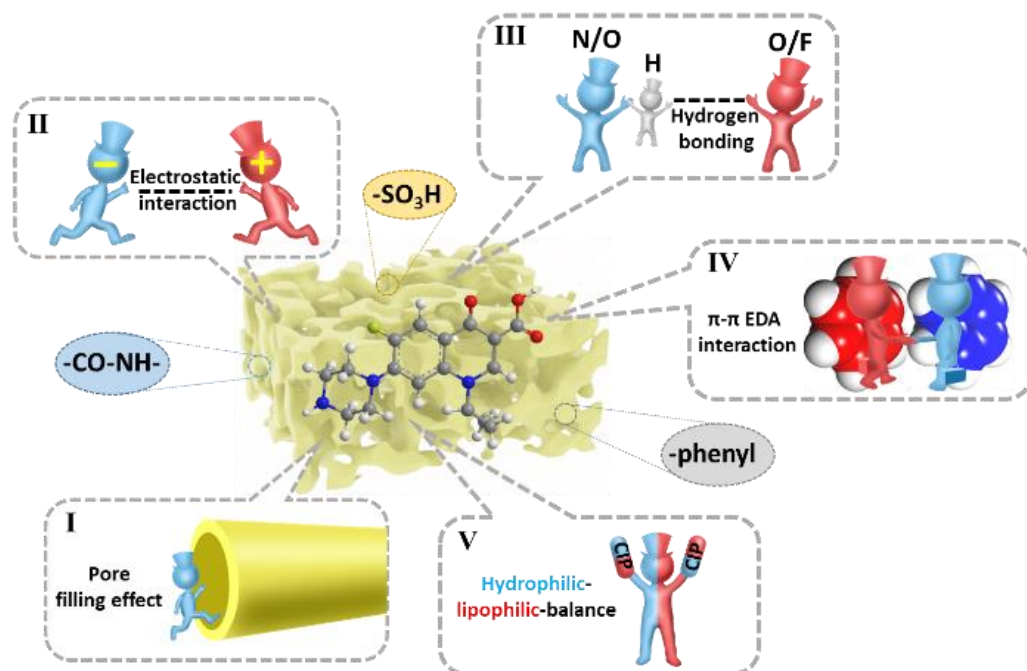

Figure 9. Mechanism of CIP adsorption by COP-SO$_3$H.(I: the pore filling effect in polymers, II: the electrostatic interactions in the guest molecules and the framework, III: the formation of hydrogen bonding between adsorbent and adsorbate, IV: the π-π EDA interactions between CIP and COP-SO$_3$H, V: the Hydrophilic–lipophilic balance between the target pollutant and COP-SO$_3$H).

4. Experimental Materials and Methodology

4.1. Experimental Materials

Benzene-1,3,5-tricarbohydrazide (BTCH) was prepared in the laboratory using previously reported methods [58], and 4,4″-p-Terphenyldicarboxaldehyde (TPDA) and 2,5-diaminobenzenesulfonic acid (DABA) were sourced from Sinopharm Chemical Reagent Co. Ltd. (Shanghai, China).

4.2. COP-SO$_3$H Characterization

The microstructures of COP-SO$_3$H were observed using scanning electron microscopy (SEM, ZEISS, Gemini Sigma 300, Oberkochen, Germany) and transmission electron micro-

scope (TEM, FEI, Tecnai F20, Hillsboro, OR, USA). The morphological changes in the raw material COP-SO$_3$H and the COP-SO$_3$H material after adsorption and subsequent cleaning were examined using a Zeiss Sigma 300 microscope. Thermogravimetric analysis of COP-SO$_3$H was conducted using a NETZSCH STA 2500 thermal analyzer (Free State of Bavaria, Germany) at a heating rate of 10 °C·min^{-1} under a protective N$_2$ atmosphere. XRD spectra in the 4–40° range were acquired using a powder X-ray diffractometer (ESCALAB 250Xi, Thermo Fisher Scientific, Waltham, MA, USA). Solid-state 13C cross-polarization/magic angle spinning nuclear magnetic resonance (CP/MAS NMR) spectra were recorded at 5 kHz. Elemental analyses of C,H,N, and S were conducted using an Elementar Vario Micro analyzer. The FT-IR of COP-SO$_3$H, which was pressed into KBr powder, was performed within the range of 400–4000 cm^{-1} using a Nexus 410 infrared spectrometer. X-ray photoelectron spectroscopy (XPS) was performed using an ESCALAB 250Xi instrument. The N$_2$-specific surface area of COP-SO$_3$H was measured using an Autosorb iQ2 instrument (QuantaChrome Instruments Corp., Boynton Beach, FL, USA). Additionally, the point of zero charge of COP-SO$_3$H at different pH values was determined by the pH drift method using a zeta potential meter (Zetasizer Nano ZS90, Malvern Panalytical, Malvern, UK). Furthermore, the initial and equilibrium concentrations of CIP were measured at a wavelength of 271 nm using a Shimadzu UV-2550 spectrophotometer.

4.3. Synthesis of COP-SO$_3$H

BTCH (0.2 mmol, 50.4 mg), TPDA (0.6 mmol, 171.8 mg), and DABA (0.3 mmol, 56.5 mg) were weighed and added to a headspace vial containing dimethyl sulfoxide (DMSO, 5 mL) as a solvent. The three compounds were thoroughly mixed, heated to 100 °C, and maintained for 15 min, to yield a red polymer. The polymer was transferred to a dialysis bag and dialyzed with distilled water to remove the organic solvent. After dialysis, the material was transferred to a conical flask and freeze-dried. The resulting pale-red powder was COP-SO$_3$H.

4.4. Adsorption Experiments

For all the experiments, CIP was dissolved in distilled water to obtain the required solution. In each instance, COP-SO$_3$H was mixed with an antibiotic in a 50 mL plastic centrifuge tube and agitated in a gas bath shaker at 150 r·min^{-1}. Periodically, a specific volume of supernatant was extracted via centrifugation. The remaining CIP concentration was determined via ultraviolet–visible spectrophotometry at λ = 271 nm. Different amounts of COP-SO$_3$H (0.25, 0.5, 1, 1.5, and 2 g·L^{-1}) were mixed in a 20 mL CIP solution with an initial concentration of 10 mg·L^{-1} to examine the effects of adsorbent dosage on the adsorption properties of COP-SO$_3$H. The effect of the initial pH on the adsorption of CIP by COP-SO$_3$H was investigated at an initial CIP concentration of 10 mg·L^{-1}, COP-SO$_3$H addition of 1 g·L^{-1}, and pH values ranging from 2 to 10. At 20 °C, adsorption kinetics experiments were performed by mixing 1 g·L^{-1} of COP-SO$_3$H with a CIP solution (40 mL volume, pH = 6, initial concentrations of 10, 20, and 30 mg·L^{-1}) in a 50 mL centrifuge tube. Intermittent adsorption experiments were conducted at 10, 20, and 30 °C by mixing 1 g·L^{-1} COP-SO$_3$H with 40 mL of CIP (concentrations of 10, 20, 30, 50, 80, 110, and 170 mg·L^{-1}) in a 50 mL centrifuge tube. This was performed to explore the isothermal adsorption characteristics of CIP on COP-SO$_3$H. Using a CIP solution without added ions as a control, the influence of ion competition on the adsorption of CIP by COP-SO$_3$H was studied by adding ions, such as Na$^+$, K$^+$, Ca^{2+}, Mg^{2+}, Cl$^-$, CO$_3^{2-}$, HCO$_3^-$, and SO$_4^{2-}$ at a concentration of 10 mM. Additionally, the effects of different concentrations of Na$^+$ and Ca^{2+} (ranging from 0 to 50 mg·L^{-1}) on the adsorption of CIP by COP-SO$_3$H were explored. The adsorption quantity of the COP-SO$_3$H material at time t, denoted as q_t (mg·L^{-1}), equilibrium adsorption quantity, denoted as q_e (mg·L^{-1}), and removal efficiency (%) were determined using the following formulas [59,60]:

$$q_t = \frac{V(C_0 - C_t)}{m} \tag{12}$$

$$q_e = \frac{V(C_0 - C_e)}{m} \tag{13}$$

$$E(\%) = \frac{C_0 - C_e}{C_0} \times 100\% \tag{14}$$

where C_0 (mg·L^{-1}) is the initial concentration of CIP; C_e (mg·L^{-1}) and C_t (mg·L^{-1}) are the concentrations of CIP at equilibrium and at adsorption time t, respectively; m (g) represents the mass of COP-SO$_3$H added; and V (L) is the volume of the CIP solution.

5. Conclusions

In summary, based on the three monomers, BTCH, TPDA, and DABA, a ternary covalent organic polymer (COP-SO$_3$H) anchored with -SO$_3$H was designed using the Schiff reaction and a multicomponent solvothermal method. This design endowed the polymer with porous structural characteristics, abundant π-conjugated phenyl rings, and abundant CO-NH and SO$_3$H functional groups, which facilitated the removal of CIP from water. The experimental results showed that COP-SO$_3$H achieved a good adsorption performance over a wide pH range of 4–10. The adsorption process followed pseudo-second-order kinetics and followed the Langmuir model. Moreover, BET, XPS, FT-IR, and zeta potential analyses indicated that the adsorption mechanism involved pore-filling effects, electrostatic interactions, hydrogen bonding, π-π EDA interactions, and the hydrophilic–lipophilic balance. After five cycles, the material maintained a removal efficiency of >75%, confirming the reusability of COP-SO$_3$H. The present study investigates the adsorption behavior of COP-SO$_3$H on FQs (using CIP as a representative) in aqueous environments, thereby expanding the application potential of designed functionalized COPs for selective pollutant removal and water environment remediation.

Author Contributions: Z.W. (Zhuoran Wang): Conceptualization, Investigation, Formal analysis, Visualization, and Writing—review and editing. C.Q.: Conceptualization, Resources, and Validation. D.Z.: Investigation. Z.W. (Ziheng Wang): Data curation. D.M.: Formal analysis. All authors have read and agreed to the published version of the manuscript.

Institutional Review Board Statement: Not applicable.

Informed Consent Statement: Not applicable.

Data Availability Statement: Available on demand.

Conflicts of Interest: The authors declare no conflict of interest.

References

1. Ezelarab, H.A.A.; Abbas, S.H.; Hassan, H.A.; Abuo-Rahma, G.E.A. Recent Updates of Fluoroquinolones as Antibacterial Agents. *Arch. Pharm.* **2018**, *351*, 1800141. [CrossRef]
2. Inyinbor, A.A.; Bello, O.S.; Fadiji, A.E.; Inyinbor, H.E. Threats from Antibiotics: A Serious Environmental Concern. *J. Environ. Chem. Eng.* **2018**, *6*, 784–793. [CrossRef]
3. Zhang, H.Q.; Jia, Y.Y.; Khanal, S.K.; Lu, H.; Fang, H.T.; Zhao, Q. Understanding the Role of Extracellular Polymeric Substances on Ciprofloxacin Adsorption in Aerobic Sludge, Anaerobic Sludge, and Sulfate-Reducing Bacteria Sludge Systems. *Environ. Sci. Technol.* **2018**, *52*, 6476–6486. [CrossRef]
4. Zhang, B.P.; Han, X.L.; Gu, P.J.; Fang, S.Q.; Bai, J. Response Surface Methodology Approach for Optimization of Ciprofloxacin Adsorption Using Activated Carbon Derived from the Residue of Desilicated Rice Husk. *J. Mol. Liq.* **2017**, *238*, 316–325. [CrossRef]
5. Danner, M.C.; Robertson, A.; Behrends, V.; Reiss, J. Antibiotic Pollution in Surface Fresh Waters: Occurrence and Effects. *Sci. Total Environ.* **2019**, *664*, 793–804. [CrossRef]
6. Ahmadzadeh, S.; Asadipour, A.; Pournamdari, M.; Behnam, B.; Rahimi, H.R.; Dolatabadi, M. Removal of Ciprofloxacin from Hospital Wastewater Using Electrocoagulation Technique by Aluminum Electrode: Optimization and Modelling through Response Surface Methodology. *Process Saf. Environ. Prot.* **2017**, *109*, 538–547. [CrossRef]

7. Bajpai, S.K.; Bajpai, M.; Rai, N. Sorptive Removal of Ciprofloxacin Hydrochloride from Simulated Wastewater Using Sawdust: Kinetic Study and Effect of pH. *Water SA* **2012**, *38*, 673–682. [CrossRef]

8. Maul, J.D.; Schuler, L.J.; Belden, J.B.; Whiles, M.R.; Lydy, M.J. Effects of the Antibiotic Ciprofloxacin on Stream Microbial Communities and Detritivorous Macroinvertebrates. *Environ. Toxicol. Chem.* **2006**, *25*, 1598–1606. [CrossRef] [PubMed]

9. Rutgersson, C.; Fick, J.; Marathe, N.; Kristiansson, E.; Janzon, A.; Angelin, M.; Johansson, A.; Shouche, Y.; Flach, C.F.; Larsson, D.G.J. Fluoroquinolones and Qnr Genes in Sediment, Water, Soil, and Human Fecal Flora in an Environment Polluted by Manufacturing Discharges. *Environ. Sci. Technol.* **2014**, *48*, 7825–7832. [CrossRef] [PubMed]

10. Sim, W.J.; Lee, J.W.; Lee, E.S.; Shin, S.K.; Hwang, S.R.; Oh, J.E. Occurrence and Distribution of Pharmaceuticals in Wastewater from Households, Livestock Farms, Hospitals and Pharmaceutical Manufactures. *Chemosphere* **2011**, *82*, 179–186. [CrossRef] [PubMed]

11. Igwegbe, C.A.; Oba, S.N.; Aniagor, C.O.; Adeniyi, A.G.; Ighalo, J.O. Adsorption of Ciprofloxacin from Water: A Comprehensive Review. *J. Ind. Eng. Chem.* **2021**, *93*, 57–77. [CrossRef]

12. Zeng, Y.M.; Zhou, G.M.; He, D.D.; Peng, G.L. Catalytic Degradation of Ciprofloxacin in Aqueous Solution by Peroxymonosulfate Activated with a Magnetic $CuFe_2O_4$@Biochar Composite. *Int. J. Mol. Sci.* **2023**, *24*, 5702. [CrossRef]

13. Mohammed, S.J.; Ridha, M.J.M.; Abed, K.M.; Elgharbawy, A.A.M. Removal of Levofloxacin and Ciprofloxacin from Aqueous Solutions and an Economic Evaluation Using the Electrocoagulation Process. *Int. J. Environ. Anal. Chem.* **2021**, *103*, 3801–3819. [CrossRef]

14. Babic, S.; Perisa, M.; Skoric, I. Photolytic Degradation of Norfloxacin, Enrofloxacin and Ciprofloxacin in Various Aqueous Media. *Chemosphere* **2013**, *91*, 1635–1642. [CrossRef] [PubMed]

15. Liao, X.B.; Li, B.X.; Zou, R.S.; Dai, Y.; Xie, S.G.; Yuan, B.L. Biodegradation of Antibiotic Ciprofloxacin: Pathways, Influential Factors, and Bacterial Community Structure. *Environ. Sci. Pollut. Res.* **2016**, *23*, 7911–7918. [CrossRef] [PubMed]

16. Yao, J.J.; Deng, Y.; Li, D.S.; Li, H.P.; Yang, H.Y. Role of Magnetic Substances in Adsorption Removal of Ciprofloxacin by Gamma Ferric Oxide and Ferrites Co-Modified Carbon Nanotubes. *J. Colloid Interface Sci.* **2023**, *638*, 872–881. [CrossRef]

17. Das, S.; Sengupta, S. Sustainable Removal of Antibiotic Drugs from Wastewater Using Different Adsorbents—A Concise Review. *Water Conserv. Sci. Eng.* **2023**, *8*, 10. [CrossRef]

18. Thommes, M.; Cychosz, K. Recent Advances in the Textural Characterization of Hierarchically Structured Nanoporous Materials. In *Electrochemical Society Meeting Abstracts 233*; The Electrochemical Society, Inc.: Pennington, NJ, USA, 2017; p. 2374.

19. Tian, Y.Y.; Zhu, G.S. Porous Aromatic Frameworks (PAFs). *Chem. Rev.* **2020**, *120*, 8934–8986. [CrossRef] [PubMed]

20. Zhang, X.T.; Shen, J.C.; Zhuo, N.; Tian, Z.Q.; Xu, P.R.; Yang, Z.; Yang, W.B. Interactions between Antibiotics and Graphene-Based Materials in Water: A Comparative Experimental and Theoretical Investigation. *ACS Appl. Mater. Interfaces* **2016**, *8*, 24273–24280. [CrossRef] [PubMed]

21. Van de Voorde, B.; Bueken, B.; Denayer, J.; De Vos, D. Adsorptive Separation on Metal-Organic Frameworks in the Liquid Phase. *Chem. Soc. Rev.* **2014**, *43*, 5766–5788. [CrossRef] [PubMed]

22. Li, Y.; Yang, C.X.; Qian, H.L.; Zhao, X.; Yan, X.P. Carboxyl-Functionalized Covalent Organic Frameworks for the Adsorption and Removal of Triphenylmethane Dyes. *ACS Appl. Nano Mater.* **2019**, *2*, 7290–7298. [CrossRef]

23. Wang, T.A.; Azhar, I.F.; Yang, Y.T.; Lu, Y.; Tian, Y.Y.; Gao, N.; Cui, F.C.; Yang, L.; Jing, X.F.; Zhu, G.S. Fine-Tuned Mesoporous Covalent Organic Frameworks for Highly Efficient Low Molecular-Weight Proteins Separation. *Nano Res.* **2022**, *15*, 4569–4574. [CrossRef]

24. Kuhn, P.; Antonietti, M.; Thomas, A. Porous, Covalent Triazine-Based Frameworks Prepared by Ionothermal Synthesis. *Angew. Chem. Int. Ed.* **2008**, *47*, 3450–3453. [CrossRef]

25. Wang, T.A.; Du, Y.Y.; Yang, Y.T.; Jing, X.F.; Zhu, G.S. Imidazolium-Functionalized Ionic Porous Aromatic Frameworks For CO_2 Capture and in Situ Conversion. *Ind. Eng. Chem. Res.* **2022**, *61*, 7284–7291. [CrossRef]

26. Tan, W.; Xu, X.Y.; Lv, Y.X.; Lei, W.J.; Hu, K.; Ye, F.G.; Zhao, S.L. Sulfonic Acid Functionalized Hierarchical Porous Covalent Organic Frameworks as a SALDI-TOF MS Matrix for Effective Extraction and Detection of Paraquat and Diquat. *J. Colloid Interface Sci.* **2021**, *603*, 172–181. [CrossRef] [PubMed]

27. Pan, J.L.; Jia, S.; Li, G.K.; Hu, Y.L. Organic Building Block Based Microporous Network Snw-1 Coating Fabricated by Multi Layer Interbridging Strategy for Efficient Enrichment of Trace Volatiles. *Anal. Chem.* **2015**, *87*, 3373–3381. [CrossRef] [PubMed]

28. Chandra, S.; Kundu, T.; Dey, K.; Addicoat, M.; Heine, T.; Banerjee, R. Interplaying Intrinsic and Extrinsic Proton Conductivities in Covalent Organic Frameworks. *Chem. Mater.* **2016**, *28*, 1489–1494. [CrossRef]

29. Zhong, H.; Fu, Z.H.; Taylor, J.M.; Xu, G.; Wang, R.H. Inorganic Acid-Impregnated Covalent Organic Gels as High-Performance Proton-Conductive Materials at Subzero Temperatures. *Adv. Funct. Mater.* **2017**, *27*, 1701465. [CrossRef]

30. Zhang, C.J.; Li, G.K.; Zhang, Z.M. A Hydrazone Covalent Organic Polymer Based Micro-Solid Phase Extraction for Online Analysis of Trace Sudan Dyes in Food Samples. *J. Chromatogr. A* **2015**, *1419*, 1–9. [CrossRef]

31. Jia, S.Z.; Pan, H.Y.; Lin, Q.; Wang, X.S.; Li, C.G.; Wang, M.; Shi, Y.Y. Study on the Preparation and Mechanism of Chitosan-Based Nano-Mesoporous Carbons by Hydrothermal Method. *Nanotechnology* **2020**, *31*, 365604. [CrossRef]

32. Qian, C.; Zhou, W.Q.; Qiao, J.S.; Wang, D.D.; Li, X.; Teo, W.L.; Shi, X.Y.; Wu, H.W.; Di, J.; Wang, H.; et al. Linkage Engineering by Harnessing Supramolecular Interactions to Fabricate 2d Hydrazone-Linked Covalent Organic Framework Platforms toward Advanced Catalysis. *J. Am. Chem. Soc.* **2020**, *142*, 18138–18149. [CrossRef]

33. Advani, J.H.; Singh, A.S.; Noor-ul, H.K.; Bajaj, H.C.; Biradar, A.V. Black yet Green: Sulfonic Acid Functionalized Carbon as a Catalyst for Highly Selective Isomerization of α-Pinene Oxide to Trans-Carveol. *Appl. Catal. B Environ.* **2019**, *268*, 118456. [CrossRef]

34. Kilic, D.; Sevim, M.; Eroglu, Z.; Metin, O.; Karaca, S. Strontium Oxide Modified Mesoporous Graphitic Carbon Nitride/Titanium Dioxide Nanocomposites (SrO-mpg-CN/TiO$_2$) as Efficient Heterojunction Photocatalysts for the Degradation of Tetracycline in Water. *Adv. Powder Technol.* **2021**, *32*, 2743–2757. [CrossRef]

35. Chandrasekaran, A.; Patra, C.; Narayanasamy, S.; Subbiah, S. Adsorptive Removal of Ciprofloxacin and Amoxicillin from Single and Binary Aqueous Systems Using Acid-Activated Carbon from *Prosopis juliflora*. *Environ. Res.* **2020**, *188*, 109825. [CrossRef]

36. Subramaniyasharma, S.; Shanmugam, S.R.; Bhuvaneswari, V.; Ponnusami, V.; Rangabhashiyam, S. Pyrolysis of an Invasive Weed *Prosopis juliflora* Wood Biomass for the Adsorptive Removal of Ciprofloxacin. *Biomass Convers. Biorefin.* **2023**, *13*, 9435–9450. [CrossRef]

37. Liang, C.H.; Zhang, X.D.; Feng, P.; Chai, H.X.; Huang, Y.M. ZIF-67 Derived Hollow Cobalt Sulfide as Superior Adsorbent for Effective Adsorption Removal of Ciprofloxacin Antibiotics. *Chem. Eng. J.* **2018**, *344*, 95–104. [CrossRef]

38. Lu, D.W.; Xu, S.; Qiu, W.; Sun, Y.; Liu, X.B.; Yang, J.J.; Ma, J. Adsorption and Desorption Behaviors of Antibiotic Ciprofloxacin on Functionalized Spherical Mcm-41 for Water Treatment. *J. Clean. Prod.* **2020**, *264*, 121644. [CrossRef]

39. Jiang, S.B.; Yu, T.F.; Xia, R.; Wang, X.; Gao, M.Z. Realization of of Super High Adsorption Capability of 2D δ-MnO$_2$/GO through Intra-Particle Diffusion. *Mater. Chem. Phys.* **2019**, *232*, 374–381. [CrossRef]

40. Zeng, W.; Liu, Y.G.; Hu, X.J.; Liu, S.B.; Zeng, G.M.; Zheng, B.H.; Jiang, L.H.; Guo, F.Y.; Ding, Y.; Xu, Y. Decontamination of Methylene Blue from Aqueous Solution by Magnetic Chitosan Lignosulfonate Grafted with Graphene Oxide: Effects of Environmental Conditions and Surfactant. *RSC Adv.* **2016**, *6*, 19298–19307. [CrossRef]

41. Zhao, Z.; Liang, B.; Wang, M.; Yang, Q.; Su, M.; Liang, S.X. Microporous Carbon Derived from Hydroxyl Functionalized Organic Network for Efficient Adsorption of Flumequine: Adsorption Mechanism and Application Potentials. *Chem. Eng. J.* **2022**, *427*, 130943. [CrossRef]

42. Ho, Y.S.; Chiu, W.T.; Wang, C.C. Regression Analysis for the Sorption Isotherms of Basic Dyes on Sugarcane Dust. *Bioresour. Technol.* **2005**, *96*, 1285–1291. [CrossRef]

43. Shang, J.G.; Kong, X.R.; He, L.L.; Li, W.H.; Liao, Q.J.H. Low-Cost Biochar Derived from Herbal Residue: Characterization and Application for Ciprofloxacin Adsorption. *Int. J. Environ. Sci. Technol.* **2016**, *13*, 2449–2458. [CrossRef]

44. Calagui, M.J.C.; Senoro, D.B.; Kan, C.C.; Salvacion, J.W.L.; Futalan, C.M.; Wan, M.W. Adsorption of Indium(III) Ions from Aqueous Solution Using Chitosan-Coated Bentonite Beads. *J. Hazard. Mater.* **2014**, *277*, 120–126. [CrossRef]

45. Chen, A.H.; Huang, Y.Y. Adsorption of Remazol Black 5 from Aqueous Solution by the Templated Crosslinked-Chitosans. *J. Hazard. Mater.* **2010**, *177*, 668–675. [CrossRef]

46. Avci, A.; Inci, I.; Baylan, N. A Comparative Adsorption Study with Various Adsorbents for the Removal of Ciprofloxacin Hydrochloride from Water. *Water Air Soil Pollut.* **2019**, *230*, 250. [CrossRef]

47. Zhao, P.P.; Wu, Y.Q.; Yu, F. Experimental Data and Modeling the Adsorption-Desorption and Mobility Behavior of Ciprofloxacin in Sandy Silt Soil. *Water* **2022**, *14*, 1728. [CrossRef]

48. Chang, F.; Memon, N.; Memon, S.; Chang, A.S. Selective Adsorption of Emerging Contaminants from Aqueous Solution Using Cu-Based Composite by Solvothermal. *Int. J. Environ. Sci. Technol.* **2022**, *19*, 11161–11168. [CrossRef]

49. Chang, F.; Memon, N.; Memon, S.; Chang, A.S. Removal of Emerging Contaminants from Water by Using Fe-MOF Composite as a Sorbent. *J. Iran Chem. Soc.* **2021**, *18*, 3249–3255. [CrossRef]

50. Kaya, G.G.; Aznar, E.; Deveci, H.; Martinez-Manez, R. Low-Cost Silica Xerogels as Potential Adsorbents for Ciprofloxacin Removal. *Sustain. Chem. Pharm.* **2021**, *22*, 100483. [CrossRef]

51. Li, X.N.; Wang, W.Q.; Dou, J.; Gao, J.S.; Chen, S.; Quan, X.; Zhao, H.M. Dynamic Adsorption of Ciprofloxacin on Carbon Nanofibers: Quantitative Measurement by in Situ Fluorescence. *J. Water Process. Eng.* **2016**, *9*, E14–E20. [CrossRef]

52. Wang, C.J.; Li, Z.H.; Jiang, W.T. Adsorption of Ciprofloxacin on 2:1 Dioctahedral Clay Minerals. *Appl. Clay Sci.* **2011**, *53*, 723–728. [CrossRef]

53. Velusamy, K.; Periyasamy, S.; Kumar, P.S.; Jayaraj, T.; Krishnasamy, R.; Sindhu, J.; Sneka, D.; Subhashini, B.; Vo, D.V.N. Analysis on the Removal of Emerging Contaminant from Aqueous Solution Using Biochar Derived from Soap Nut Seeds. *Environ. Pollut.* **2021**, *287*, 117632. [CrossRef] [PubMed]

54. Chang, S.H.; Lu, C.C.; Lin, C.W.; Wang, K.S.; Lee, M.W.; Liu, S.H. Waste Expanded Polystyrene Modified with H$_2$SO$_4$/Biodegradable Chelating Agent for Reuse: As a Highly Efficient Adsorbent to Remove Fluoroquinolone Antibiotic from Water. *Chemosphere* **2022**, *288*, 132619. [CrossRef]

55. Jin, J.H.; Yang, Z.H.; Xiong, W.P.; Zhou, Y.Y.; Xu, R.; Zhang, Y.R.; Cao, J.; Li, X.; Zhou, C.Y. Cu and Co Nanoparticles Co-Doped MIL-101 as a Novel Adsorbent for Efficient Removal of Tetracycline from Aqueous Solutions. *Sci. Total Environ.* **2019**, *650*, 408–418. [CrossRef]

56. Geng, K.; He, T.; Liu, R.; Dalapati, S.; Tan, K.T.; Li, Z.; Tao, S.; Gong, Y.; Jiang, Q.; Jiang, D. Covalent Organic Frameworks: Design, Synthesis, and Functions. *Chem. Rev.* **2020**, *120*, 8814–8933. [CrossRef]

57. Zhao, W.J.; Zuo, H.Y.; Guo, Y.; Liu, K.J.; Wang, S.; He, L.J.; Jiang, X.M.; Xiang, G.Q.; Zhang, S.S. Porous Covalent Triazine-Terphenyl Polymer as Hydrophilic-Lipophilic Balanced Sorbent for Solid Phase Extraction of Tetracyclines in Animal Derived Foods. *Talanta* **2019**, *201*, 426–432. [CrossRef]

58. Lin, L.; Guan, H.D.; Zou, D.L.; Dong, Z.J.; Liu, Z.; Xu, F.F.; Xie, Z.G.; Li, Y.X. A Pharmaceutical Hydrogen-Bonded Covalent Organic Polymer for Enrichment of Volatile Iodine. *RSC Adv.* **2017**, *7*, 54407–54415. [CrossRef]
59. Agboola, O.S.; Bello, O.S. Enhanced Adsorption of Ciprofloxacin from Aqueous Solutions Using Functionalized Banana Stalk. *Biomass Convers. Biorefin.* **2022**, *12*, 5463–5478. [CrossRef]
60. Al-Jabari, M.H.; Sulaiman, S.; Ali, S.; Barakat, R.; Mubarak, A.; Khan, S.A. Adsorption Study of Levofloxacin on Reusable Magnetic Nanoparticles: Kinetics and Antibacterial Activity. *J. Mol. Liq.* **2019**, *291*, 111249. [CrossRef]